

## RESEARCH ARTICLE

# Microstructure and Mechanical Properties of LENS Manufactured NiTi Shape Memory Alloy After Ageing and During In-Situ SEM Tensile Test

Jan Dutkiewicz<sup>1\*</sup>, Lukasz Rogal<sup>1</sup>, Damian Kalita<sup>1</sup>, Katarzyna Berent<sup>2</sup>, Jakub Kawałko<sup>2</sup>, Anna Antolak-Dudka<sup>3</sup>, Tomasz Durejko<sup>3</sup>, Tomasz Czujko<sup>3</sup> and Eduard Cesari<sup>4</sup>

<sup>1</sup>Institute of Metallurgy and Materials Science, PAS, 25, Reymonta St., 30-059 Krakow, Poland

<sup>2</sup>Academic Centre for Materials and Nanotechnology, AGH, 30, Mickiewicza Av, Krakow, Poland

<sup>3</sup>Military University of Technology, 2, Institute of Materials Science and Engineering, Gen. S. Kaliskiego Str., 00-908, Warsaw, Poland

<sup>4</sup>Department of Physics, University of Balearic Islands, E07122, Palma de Mallorca, Spain

\*Corresponding author: Jan Dutkiewicz, Institute of Metallurgy and Materials Science, PAS, 25, Reymonta St., 30-059 Krakow, Poland, Tel: 605030696, E-mail: j.dutkiewicz@imim.pl

**Citation:** Jan Dutkiewicz, Lukasz Rogal, Damian Kalita, Katarzyna Berent, Jakub Kawałko, Anna Antolak-Dudka, Tomasz Durejko, Tomasz Czujko, Eduard Cesari (2021) Microstructure and Mechanical Properties of LENS Manufactured NiTi Shape Memory Alloy After Ageing and During In-Situ SEM Tensile Test. J Mate Sci Metall 2: 104

## Abstract

The Laser Engineered Net Shaping additive manufacturing method was used to prepare NiTi samples. In the process spherical gas atomized powder with particle size in the range of 45 – 115  $\mu\text{m}$  containing 50.08 at.% Ni was used. DSC studies showed additional peak after ageing due to  $R \rightarrow B19'$  phase formation during cooling and reverse transformation  $B19' \rightarrow R$  during heating. The martensitic transformation temperatures and the reverse transformation both increase with the ageing time. This was associated with the formation of  $\text{Ni}_4\text{Ti}_3$  precipitates during the aging, as identified for the alloy aged for 2h. As-deposited sample showed diffused DSC peaks corresponding to martensitic transformation and a good superelastic properties at RT, however after 4% strain a residual strain of 0.7% was observed. In the case of aged sample strained at room temperature a deformation of martensite occurred, whereas the super elastic properties were observed at 53°C. Samples prepared for the in-situ tensile experiment using LENS method showed a strong  $\langle 001 \rangle$  texture parallel to the build direction. In-situ tensile deformation of LENS deposited sample caused nucleation of martensitic plates first at the surface of samples; then plates nucleate preferentially at grain boundaries and propagate across grains. From the PFs measurements a following crystallographic relationship was most frequently observed:  $(001)_{B19'} \parallel (01\bar{1})_{B2}$  and  $[100]_{B19'} \parallel [100]_{B2}$ , however other variants were also observed. Existence of martensite twins on (110) and  $(10\bar{2})$  planes was observed. In-situ tensile deformation of samples aged 2h/500°C causes a decrease of plate thickness from 1.15  $\mu\text{m}$  to 0.9  $\mu\text{m}$ , what suggests participation of strain field near  $\text{Ni}_4\text{Ti}_3$  precipitates in more frequent nucleation of martensitic plates. Furthermore, more variety of crystallographic orientation relationships between cubic austenite phases like  $[010]_{B2} \parallel [100]_{B19'}$ ,  $[001]_{\text{TiNi}_{B2}} \parallel [1\bar{3}3]_{B19'}$ ,  $[001]_{B2} \parallel [011]_{B19'}$ ,  $[100]_{B2} \parallel [011]_{B19'}$  and others were observed. Some twin orientations were identified in martensite based on SEM microstructure and PF analysis, particularly at higher deformation of 8%.

**Keywords:** Additive Manufacturing, Shape Memory Alloys, NiTi, Martensitic Transformation, Super Elasticity, In-Situ Studies

## Introduction

Shape memory (SM) NiTi alloys found many applications in technique such as actuators, robotic elements, sensors, valves [1] and in medical industry as stents, clamps, microvalves, microtools and others [2]. The NiTi alloys are very difficult to cast and plastically form, therefore recently several works were published concerning additive manufacturing (AM) [3-16] of these alloys such as: selective laser melting (SLM), laser engineered net shaping (LENS), and direct metal deposition (DMD). They make possible layer by layer melting and synthesis of three-dimensional (3D) products from a large variety of powdered materials.

SLM can be used to fabricate complex-shaped NiTi parts for customized applications. Additive manufacturing enables tailoring the SM response by controlling the microstructure at resolutions not possible through conventional NiTi processing methods [4,5]. In [6] in-situ X-ray diffraction was used to determine the local transformation temperature along the thermally affected regions in a laser processed NiTi thin sheet. The resulting transformation temperatures gradient was related to a local chemical compositional changes through Ni depletion and residual stress, explaining the microstructure and mechanical properties changes in additive manufactured NiTi parts. It was shown that using different process parameters, the phase transformation temperatures of SLM built NiTi entities can be directly tailored [7]. The reason behind is most likely the Ni-loss by evaporation, which increases with applied energy density. In [8-10] it has been concluded that aging is an effective method to tailor the shape memory properties and to obtain super elasticity of SLM fabricated Ni-rich NiTi alloys. In the case of NiTi/TiC composites [9] three different lenticular  $\text{Ni}_4\text{Ti}_3$  variants were found depending on precipitate diameters, causing formation of a higher interface lattice strain energy between the smaller  $\text{Ni}_4\text{Ti}_3$  variant and the matrix. Furthermore, as reported in [10] the heat treatment decreased the forward and reverse transformation temperatures of NiTi alloy, presumably due to annihilation of thermally induced defects, while the samples annealed at 500°C showed a measurable increase of the shape memory recovery, as compared to the as-processed NiTi alloy. The processing parameters used in the LENS method are noted to affect the generation of porosity as well as phase evolution of the structure [11]. The porosity reduces significantly the mechanical properties of the alloys, while the existence of precipitates along with an indication of co-existence of martensitic phase is characteristic for the alloy manufactured with the highest laser energy density i.e. NiTi [11]. Additionally, the pseudo elastic recoverability of this material is also markedly influenced by the laser energy density. In [12] a novel monolithic bionic manipulator was developed using a NiTi shape memory alloys (SMA) by laser processing, where a super elastic effect in a Ni-rich alloy was observed. The device actuation and bending were achieved by resistive heating, activating the shape memory effect (SME) in different laser processed regions. Each laser processed region has a unique phase transformation onset temperature and thermo-mechanical recovery, providing special actuation characteristics. Ni-rich NiTi alloys were also deposited using the in-situ alloying wire arc additive manufacturing (WAAM) method [13], showing a higher efficiency than the LENS method. The WAAM method however does not allow for the reproduction of details of elements with high accuracy, as is the case with the LENS method, therefore the LENS method was applied in the present work.

The characteristic phase transformation temperatures increased with the deposition current allowing to obtain 3,2% of recoverable strain [13]. It was also observed that as the deposition current increases, the intensity of the cube texture in  $\{001\}\langle 100\rangle$  sharply dropped and the intensity of Goss texture in  $\{011\}\langle 100\rangle$  decreased to almost random. Other authors also observed the effect of texture formation during LENS deposition [13,14], where the deposited material shows  $\langle 111\rangle$  fibre texture along the growth direction [14], similarly like that described for the SLM  $\text{Ni}_{50.2}\text{Ti}$  samples, where a higher number of oriented grains along the heat flow direction  $\langle 111\rangle$  was observed. As reported in [15] a high laser power causes the grain growth in the  $\langle 111\rangle$  orientation, increases the grain size, and a rectangular shape in the slice plane. In addition, defects such as pores, cracks, and residual stresses are several major problems concerning AM, which can be minimized by increasing the laser power and increasing the scanning speed to provide an appropriate melting depth. Although the possibility of crack formation is high, it was shown that the cracks are not propagating due to rapid cooling [15]. It was demonstrated that SLM fabricated samples show lower strength than the initial ingot [16], their sharp  $\{001\}$  texture along the building direction improves their super elastic response substantially. In addition, it was shown that transformation temperatures can be tailored and upon thermal treatments at temperatures 350 - 600 °C superelastic recovery up to about 5.5% can be obtained.

There are several studies on in-situ deformation of NiTi SM alloys [17-21]. The thermo-mechanical behavior of pseudoelastic NiTi bar specimens showed the localization of deformation due to formation and growth of martensitic bands during combined compression–shear [17], where the special sample geometry and the occurrence of additional shear stress can promote a mode of localized deformation. This observation was confirmed in other in-situ studies [18], where in addition it was found that for resolved shear stress, populations of grain orientations forming at tension or compression do not show significant difference. The tension-favoring orientations are close to  $\langle 111 \rangle$  and the compression favoring orientations are close to  $\langle 001 \rangle$ . The effect of texture was confirmed in [19], where NiTi wires and sheets of similar transformation temperatures and grain sizes, exhibited strong differences in their tensile and shape memory behaviors due to their different fibre textures, ie.  $\langle 111 \rangle$  B2 fibre texture along the wire axis,  $\langle 011 \rangle$  B2 fibre texture along the rolling direction. In-situ TEM studies [20,21] indicated microstructural evidence for the role of a grain boundary during the nucleation of martensite and they can act as an obstacle for the propagation of a martensite/austenite interface. In addition, it was suggested [21] that the stress-induced B2–B19' transformation increased the applied strain along  $[110]$  B2 into plates variants that are related by a  $(110)$  B2 compound twin plane.

The above literature search indicates that only in one paper [6] the X-ray diffraction in-situ method was applied to determine the local transformation temperatures in SLM manufactured alloys along the thermally affected regions, however microstructure studies of in situ deformation of AM manufactured super elastic alloys was not found. In addition, the effect of ageing of such alloys was reported to affect transformation temperatures in additive manufactured alloys [8-10, 14, 15] and therefore its effect on in-situ martensite nucleation was studied. In addition due to the reported role of preferred orientation of AM alloys [20, 21,22], its effect was also studied using in-situ EBSD analysis.

## Experimental Methods

The LENS method was used to prepare AM samples using the initial material in the form of spherical powder. During deposition, the powder was injected through the nozzles into the melt pool formed on the deposit surface by a highly focused laser beam. The deposition process was performed using the LENS MR-7 system (Optomec, USA) equipped with a 500 W fiber laser. Spherical, gas atomized powder, with particle size in the range of 45 – 115  $\mu\text{m}$  and the chemical composition: 50.08 at.% Ni, 0.01 at.% C, 0.10 at.% O, Ti balance was used. In order to obtain cylindrical samples with 20 mm diameter and the height of 10 mm, the following parameters were used: laser power 400 W, laser spot diameter 1.2 mm, working table feed rate 10 mm/min, powder flow rate 14.98 g/min, single layer thickness 0.3 mm. Moreover, the process was performed in the chamber under a purified argon atmosphere ( $\text{O}_2$  and  $\text{H}_2\text{O} < 10$  ppm). Aging at 500°C was performed for times varied from 15 min to 8h, as an example of a typical heat treatment for Ni-rich Ni-Ti alloys [22], for the additive manufactured samples. The materials were analysed in the as-deposited and aged states. The microstructural observations and Electron Backscatter Diffraction (EBSD) measurements were carried out on a FEI Versa 3D FEG scanning electron microscope (SEM) equipped with an EDAX Hikari CCD camera. The in-situ deformation studies were carried out at the room temperature using Kammrath&Weiss 5kN tensile/compression stage. The dog-bone shape samples with cross section of 1x2 mm and gauge length of 3 mm were prepared by an electrical discharge machine (EDM). The tensile testing was carried out with constant displacement rate of 3  $\mu\text{m/s}$  which resulted in strain rate of  $10^{-3} \text{ s}^{-1}$ . The detailed microstructural studies were performed using a transmission electron microscope (TEM) Tecnai FEG G2 F20 Super Twin. The thin foils for TEM observations were prepared by electropolishing 100  $\mu\text{m}$  thick discs in an electrolyte containing 10 mol.%  $\text{HClO}_4$  in methanol (voltage 20 V, temperature -20°C). The tensile tests were performed at a Shimadzu Autograph AG-X plus testing machine at strain rate  $10^{-3} \text{ s}^{-1}$ . The strain was measured using a video-extensometer TRViewX system. Tests were conducted at RT and at temperature 10 °C above  $A_f$  of the materials. The samples for the mechanical tests were cut from flat elements made using the LENS method perpendicular to the surface of the deposited layers and prepared in the same form for the tensile deformation and in-situ deformation studies. The phase transformation temperatures were investigated by a differential scanning calorimetry (DSC) using a Mettler DSC 823 instrument, with cooling/heating rate of 10 °C/min.

## Results and Discussion

### DSC Studies

In order to determine characteristic transformation temperatures and the effect of aging time at 500°C, DSC measurements were performed. At this annealing temperature, significant effects on the martensitic transformation temperatures were observed [14-16, 22]. Figure 1 shows the DSC cooling/heating curves of the material in as-deposited state as well as for alloys after various annealing times. They indicate that with increasing annealing time the martensitic transformation temperature increases and the thermal effects are split into 3 peaks resulting most probably from the R phase formation and two stage B19' martensite formation as observed earlier [22-24]. Splitting of the martensite peak results from non-homogeneity of a dislocation structure due to polygonization at the annealing temperature. Within areas of higher dislocation density martensitic transformation is shifted to lower temperatures as observed earlier in [24]. Similarly, during heating (Figure 1b) the reverse transformation temperatures increase in a similar way to those during cooling. Even the longest ageing at 500°C did not cause a degradation of the martensitic transformation as reported also earlier in conventionally prepared alloys [22-24]. Ageing of SLM prepared samples at 450°C caused also splitting of martensitic transformation temperatures and their increase with ageing time [8, 24], however the as manufactured sample showed more diffused peaks. Table 1 shows the characteristic transformation temperatures of investigated LENS prepared alloy after various annealing times at 500°C. 2 hours annealing time was chosen to study the effect of annealing on the super elastic deformation at room temperature since it changes the transformation temperature and does not degrades it.

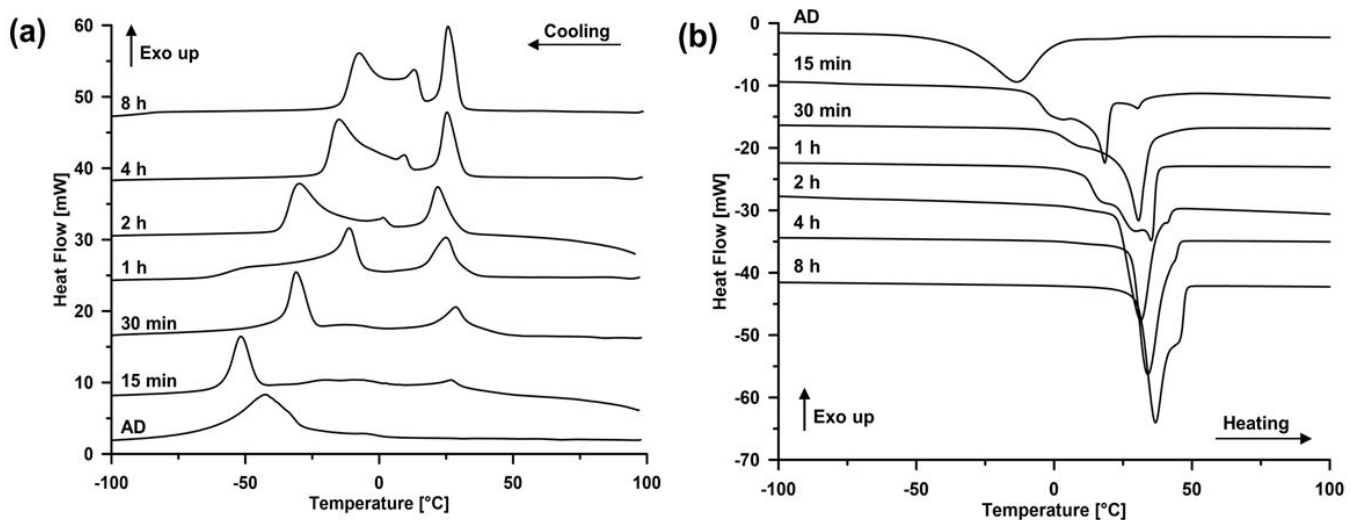


**Figure 1:** DSC (a) cooling and (b) heating curves of LENS as-deposited sample (AD) and after indicated annealing times at 500 °C

### Mechanical Properties of Superelastic NiTi Alloy

Figure 2 shows stress/strain tensile curves from the LENS prepared NiTi alloy and after additional annealing at 500°C for 2 hours. One can see that the as-prepared sample exhibits quite large superelastic behaviour after 4 % strain. Starting from about 600 MPa deformation occurs at almost constant stress indicating formation of martensite up to the end of the experiment and after unloading it remains only about 0.7% of permanent deformation. The annealed alloy shows at RT a period of constant stress deformation indicating martensite formation at lower stress near 260 MPa. At about 2.5 % strain, the stress attain the stage of either new variant formation or plastic deformation of martensite. Two stage deformation was already observed at temperatures  $M_s < T < A_f$  and was explained by reorientation of R phase [22]. After unloading only partial strain recovery can be observed and the permanent strain is finally equal to about 2.5%. Figure 3a shows a tensile curve measured from the LENS prepared sample at 42°C i.e. 10 °C above  $A_f$  and Figure 3b from the sample additionally annealed at 500°C for 2 hours and deformed at 53°C (also about 10°C above  $A_f$ ). Both samples show improved superelastic effect however in both cases about 0.5% of permanent deformation is observed after tensile deformation up to 3 or 4%.

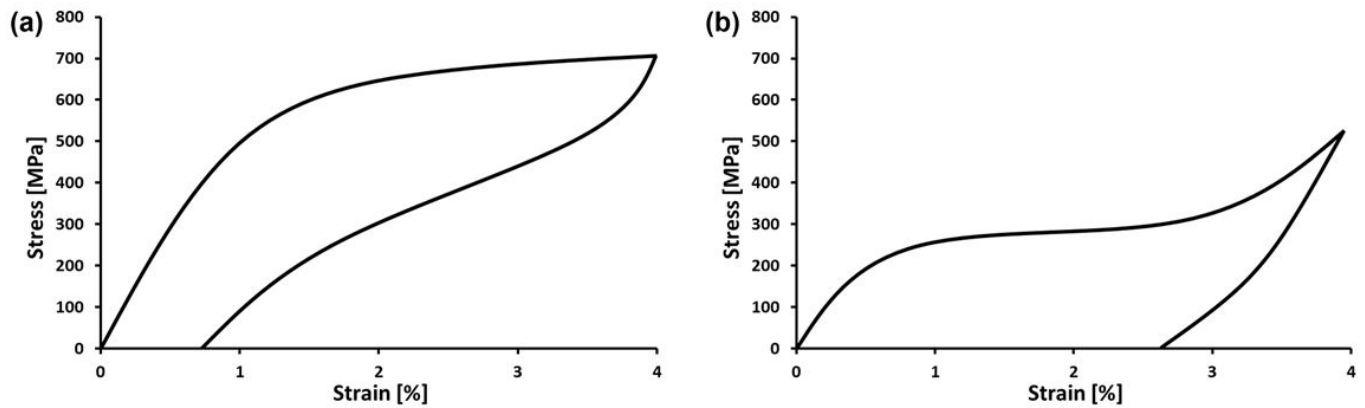


**Figure 2:** Stress/strain tensile curves measured at room temperature from (a) as prepared LENS sample; (b) sample additionally annealed at 500°C for 2 hours

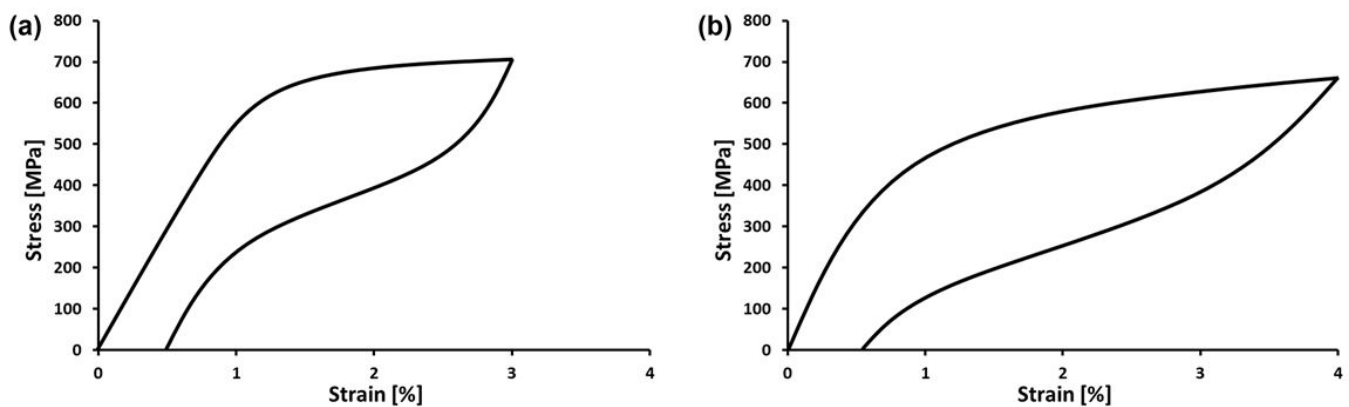


**Figure 3:** Stress/strain tensile curves measured from (a) as prepared LENS sample tested at 42°C; (b) sample additionally annealed at 500°C for 2 hours tested at 53°C

## STEM and TEM Studies of Manufactured and Aged Samples

TEM studies were performed to determine the microstructure, crystal structure and chemical composition of precipitates of as-prepared and aged alloys. Figure 4 shows STEM microstructure of as-prepared alloy with marked points where EDS spectra for the point chemical analysis were collected. The obtained results of EDS chemical analysis are presented in Figure 4 and Figure 6. One can see that the elongated particles contain more Ti (~65 at. %) and less Ni (~35 at. %), which correspond to the  $\text{NiTi}_2$  phase. Such precipitates were also observed in other works, e.g. the primary  $\text{Ni}_2\text{Ti}$  precipitates were found in the SLM manufactured NiTi samples [24]. On the other hand,  $\text{Ni}_4\text{Ti}_3$  precipitates were identified in Ni-rich  $\text{Ni}_{52.4}\text{Ti}_{47.6}$  alloy fabricated using laser-based directed energy deposition (LDED) technique [4]. However, in our case the matrix contains less Ni (50.7 at. %) what was confirmed also in other areas. Not all particles contain more titanium as results also from other analysis; some of them contain more nickel than titanium. Figure 5 confirms this observation. Both microstructures show group of particles of oval shape, while electron diffraction pattern of one of dark round particle in Figure 5a presented in Figure 5b indicate  $\text{Ti}_2\text{Ni}$  structure of zone axis [110], while SADP in Figure 5d indicate presence of  $\text{Ti}_2\text{Ni}_3$  phase of zone axis [100]. Presence of these phases was confirmed in other diffraction patterns and confirms earlier observation in [4, 9]. Formation of either titanium-rich or nickel-rich phases may be caused by a local liquid alloy composition changes due to local oxidation of titanium (in spite of pure oxygen free atmosphere more frequent  $\text{Ti}_2\text{Ni}_3$  particles were formed). In some place however formation of  $\text{Ti}_2\text{Ni}$  was observed due to a local enrichment of titanium probably due to higher melting temperature of titanium.

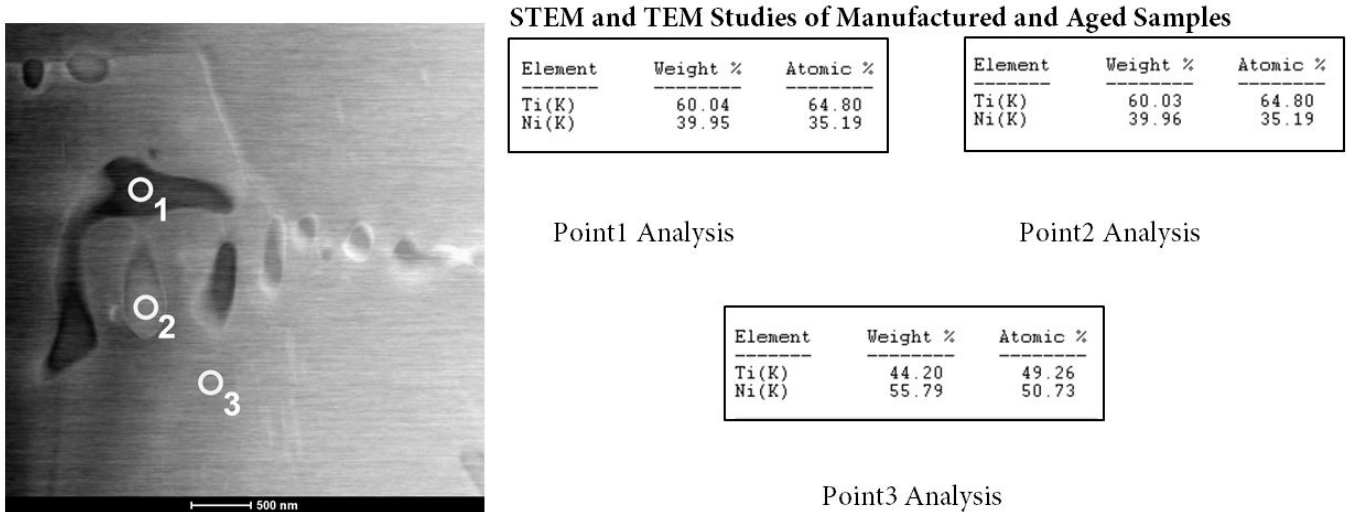


**Figure 4:** STEM microstructure from the LENS manufactured sample with marked EDS analysis points and results of the analysis in the marked points of the alloy prepared using the LENS method

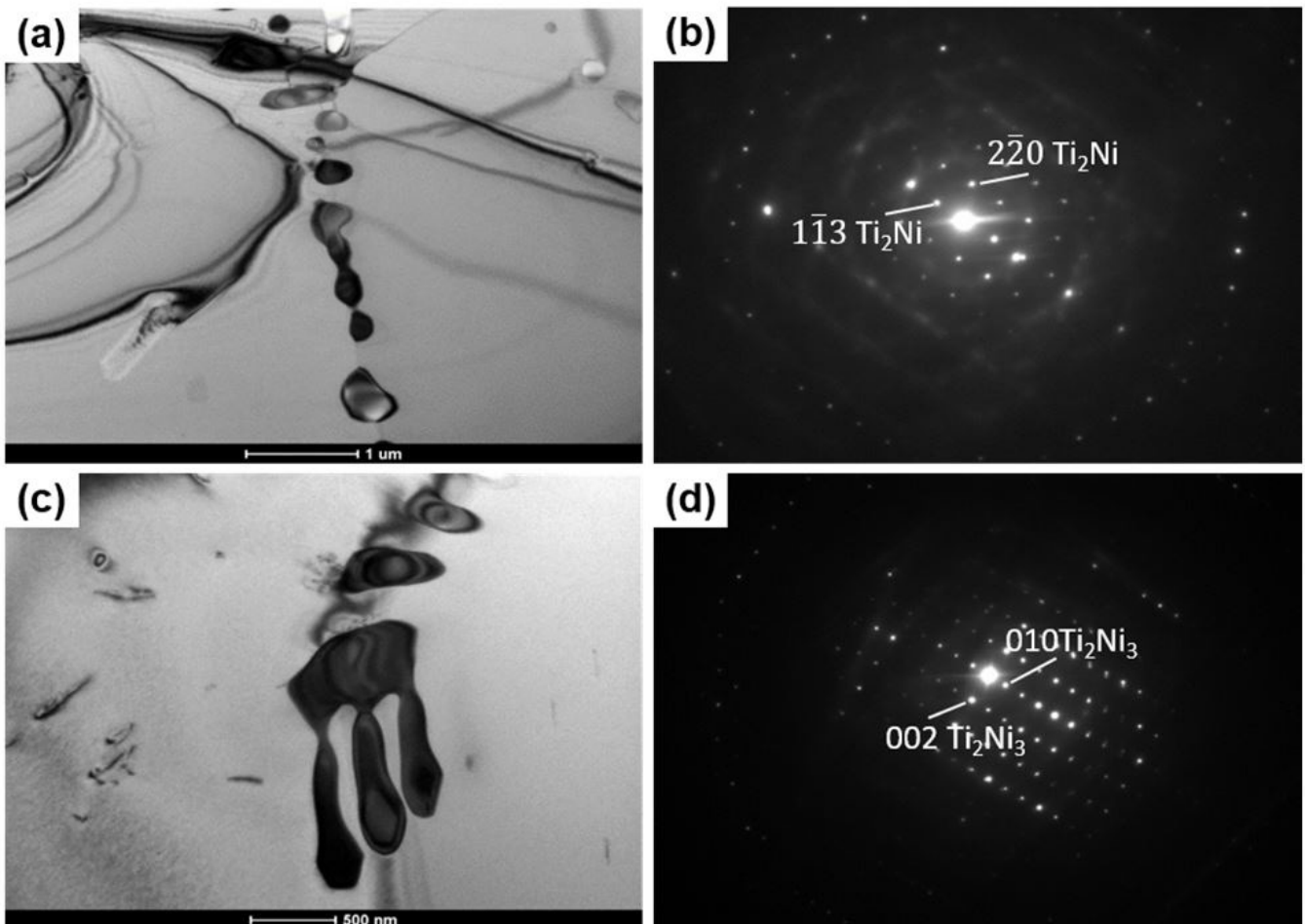
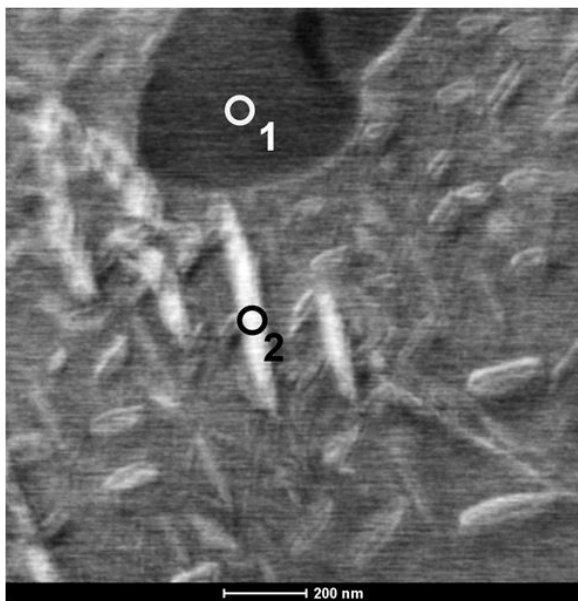


**Figure 5:** TEM microstructures from the LENS manufactured sample and Selected Area Diffraction Patterns (SADP) from the groups of oval particles present in LENS prepared samples indicating the presence of  $Ti_2Ni$  and  $Ti_2Ni_3$  particles after LENS manufacturing

Due to the extensively studied effect of ageing on the characteristic temperature changes [8-10,13,19,22,23], annealing treatment at 500°C for 2 hours was applied to induce precipitation and shifting upwards the martensitic transformation temperatures. As results from previous papers [8-10,13,19,22,23]  $M_s$  temperature should increase without degradation of transformation in NiTi, Ni-rich alloys. Figure 6 shows a STEM micrograph taken from the LENS manufactured and aged 2h/500°C sample with marked EDS microanalysis points. The obtained results are summarized in the Table 3. One can see that a large dark particle in the upper part of the micrograph marked as point 1 contains about 61 at. % of Ti and 39 at. % of Ni. It is probably a  $Ti_2Ni$  particle as identified earlier using SADP. The other elongated precipitate formed during ageing marked as point 2 contains 45 at. % Ti and 55 at. % Ni, what suggests the presence of either  $Ti_2Ni_3$  or  $Ti_3Ni_4$  precipitates identified also earlier in [22, 23]. Precipitates are clearly seen in TEM (Figure 7) micrographs similarly as observed in earlier papers [9,22,23], however the diffraction pattern allows to identify only diffused reflections from the R-phase as observed also in AM alloys [9,22].



Element	Weight %	Atomic %
Ti (K)	56.03	60.96
Ni (K)	43.96	39.03

Point1 Analysis

Element	Weight %	Atomic %
Ti (K)	39.62	44.57
Ni (K)	60.37	55.42

Point 2 Analysis

Figure 6: STEM micrograph from the sample aged 2h/500°C with the marked points and results of EDS chemical analysis

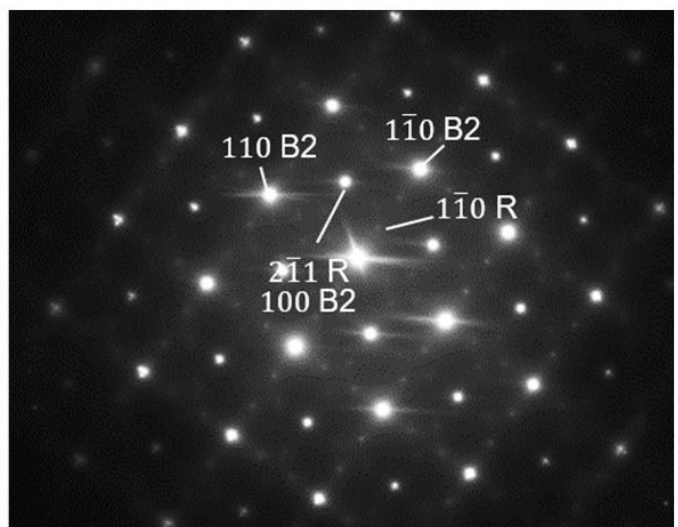
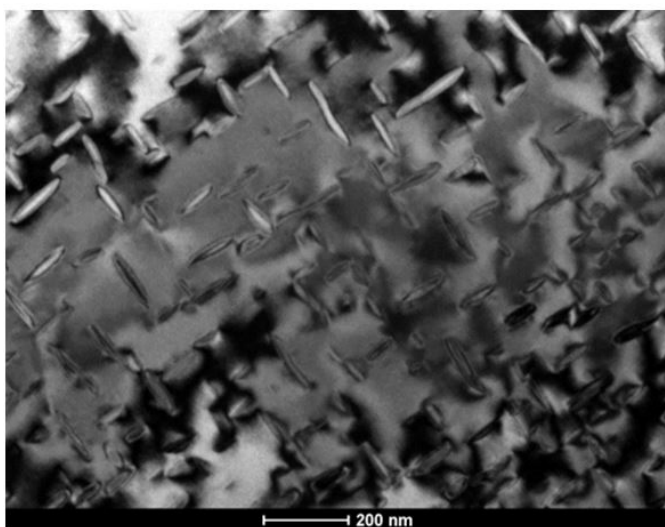
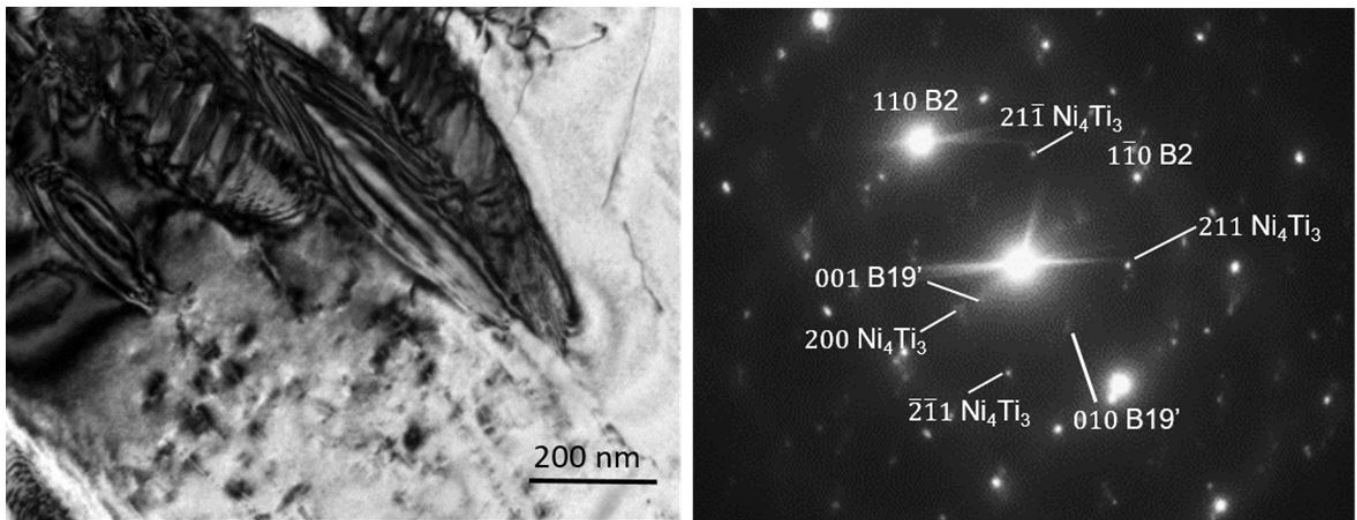


Figure 7: TEM micrograph of the LENS prepared sample aged 2h/500°C and SADP from the central area showing the presence of ordered austenite, precipitates and weak reflections of the R phase

In places where martensitic plates were formed the diffraction pattern shows more clear reflections from the B19' martensite and  $\text{Ni}_4\text{Ti}_3$  precipitates as can be seen in Figure 8. It shows TEM micrograph and SADP from the sample aged 2 hours at 500°C showing the presence of weak austenite reflections of zone axis near [001] and weak reflections from B19' martensite phase of [100] zone axis. Two systems from  $\text{Ni}_4\text{Ti}_3$  precipitates can be identified at  $[\bar{1}20]$  and [102] zone axis orientations.  $\text{Ni}_4\text{Ti}_3$  particles with size near 30 nm show strain field contrast in the austenitic phase what might affect the intensity of their diffraction patterns; however, after martensitic transformation, they show better developed diffraction spots. The formation of  $\text{Ni}_4\text{Ti}_3$  precipitates is in agreement with earlier studies of the ageing process in NiTi alloys [9] and [23] where in addition to  $\text{Ni}_4\text{Ti}_3$  also  $\text{Ni}_3\text{Ti}$  and  $\text{Ni}_3\text{Ti}_2$  precipitates were observed although in alloys containing more Ni.  $\text{Ni}_4\text{Ti}_3$  precipitates only were identified in aged near equiatomic NiTi alloys [22, 25]. Twins can be seen in the martensitic plates and can be identified as  $(20\bar{1})$  B19' martensite twins observed during earlier in-situ studies [26,34]. In other micrographs other variants of martensite twins were also observed.



**Figure 8:** TEM micrograph (a) and SADP from the area of martensite (b) taken from the LENS prepared sample aged 2h/500°C showing the presence of B2 austenite, B19' martensite and  $\text{Ni}_4\text{Ti}_3$  precipitates

### In-situ SEM Studies

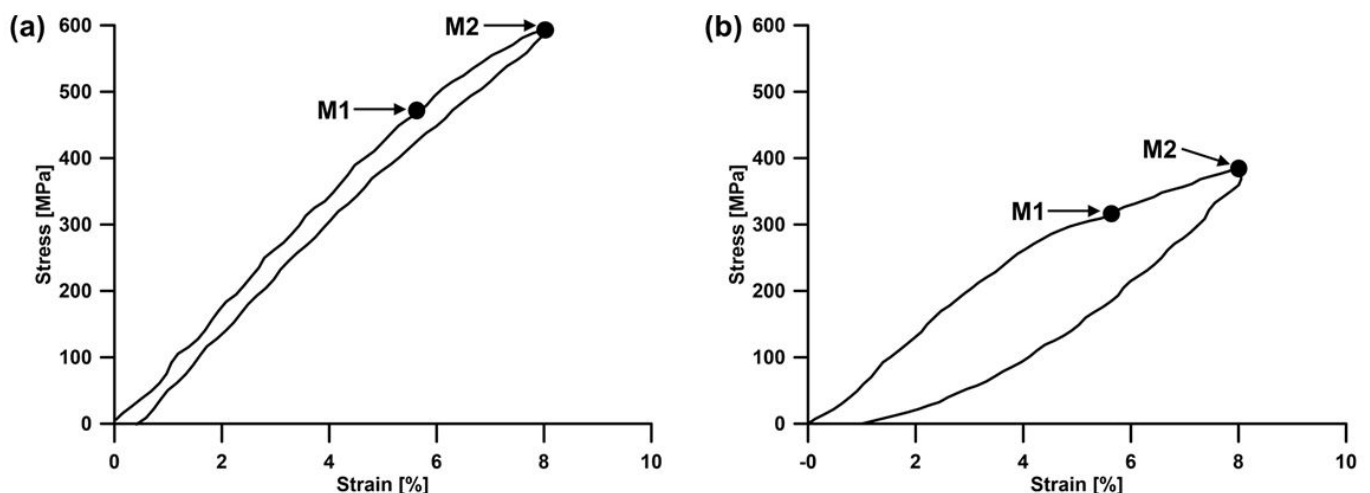


**Figure 9:** Stress/strain loading/unloading test curves taken during in-situ SEM tensile test from (a) as prepared LENS specimen (b) LENS sample aged 2h/500°C, with the marked point of EBSD measurements

Figure 9 shows stress vs. strain curves obtained using in-situ tensile attachment during SEM observation of LENS prepared tensile sample and after additional annealing at 500°C for 2 hours. One can see a different character of both curves as compared to that obtained using the tensile machine (Figure 2); the first one after preparation shows no plateau and constant strengthening up to 600 MPa, but on the other hand, it shows better strain recovery and a smaller hysteresis. The increase of tensile strain can be caused

by a sample temperature increase during the tensile test and subsequent stress increase as a result of the increase of elastic modulus of martensite with temperature as stated in [25]. It is most probably caused by a higher martensitic transformation temperature due to precipitation of Ni-rich particles  $\text{Ni}_3\text{Ti}_2$  and  $\text{Ni}_4\text{Ti}_3$  causing a decrease of nickel content in the solid solution as shown in STEM and TEM studies and in agreement with results in the literature [22,23]. The deformation of the annealed sample shows a larger distance between loading/unloading curves, which indicates a mixed character between superelastic and deformation of martensite in connection with an increase of martensite transformation temperature. Due to interruption of the tensile test for EBSD measurements and taking micrographs, the experiment took a few hours therefore temperature increase due to the formation of martensite could contribute to this effect.

SEM microstructure studies in both specimens were performed on the surface perpendicular to the growth direction as indicated by an arrow in Figure 10. It shows inverse pole figure (IPF) map of the austenite grains in the as-deposited sample from a surface of a tensile tested sample with a marked square fragment where observation was performed with increasing strain. The image shows elongated grains, with majority in purple and orange colours indicating orientation not far from [001] growth direction, as shown in the austenite unit triangle as an insert. The build direction is close to [001] as results from previous studies on additive manufactured NiTi alloys [13, 14, 16] where a cube texture was observed while an elongated grain curvature results from a nozzle movement during deposition.

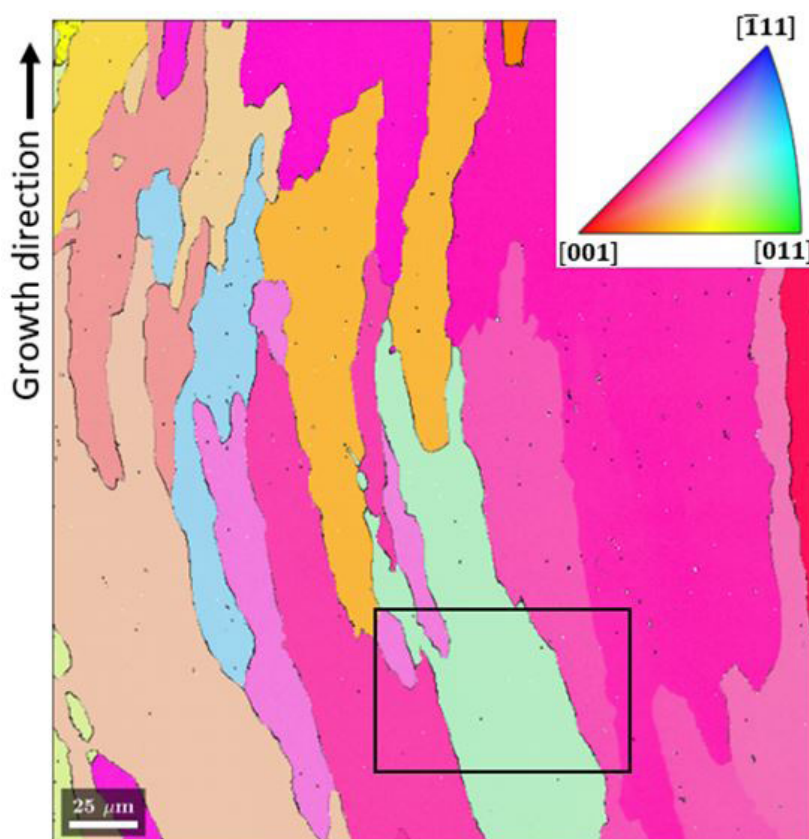
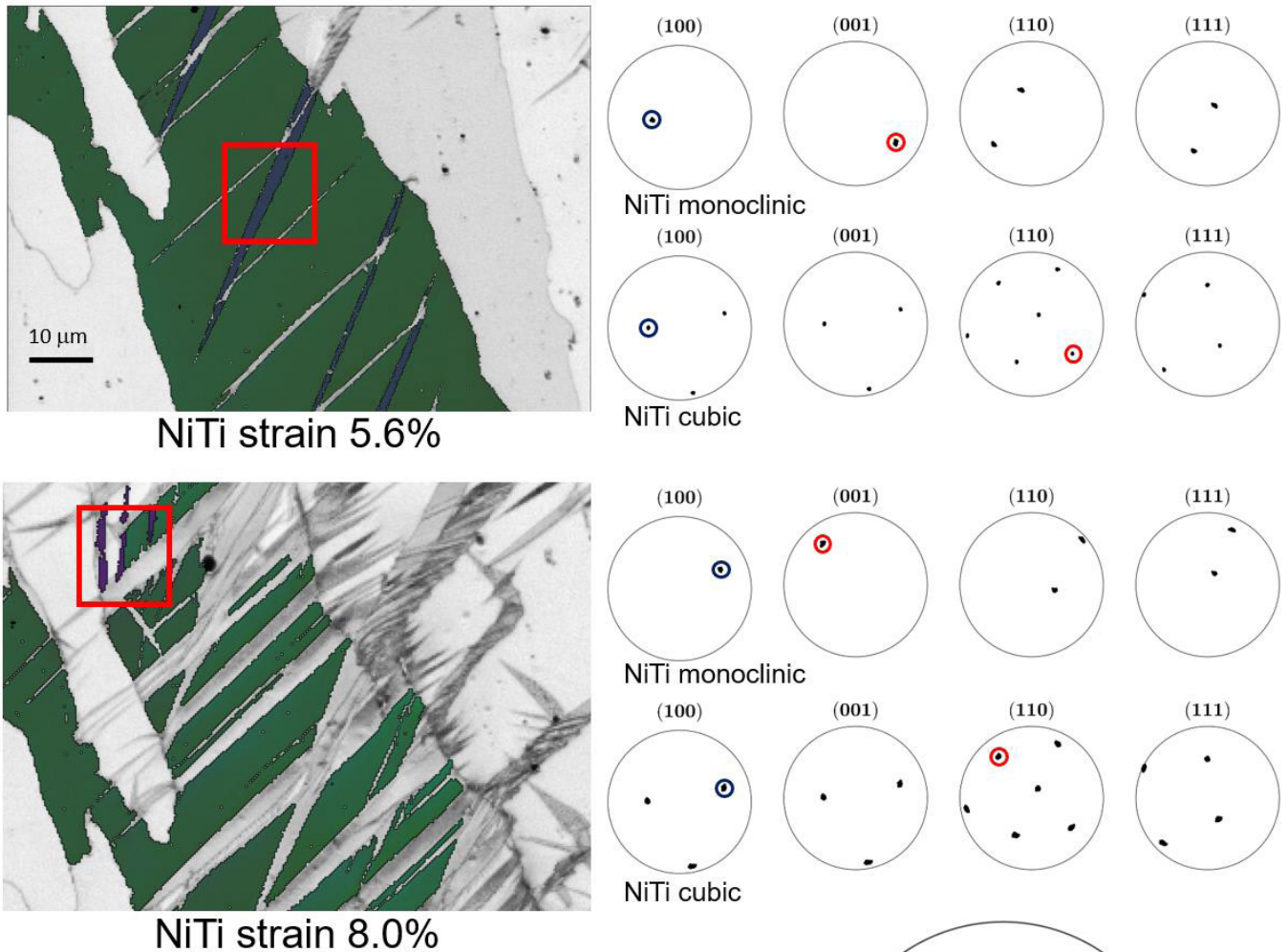


**Figure 10:** IPF map of the initial state of a tensile sample with a square marked fragment where observation was performed with increasing strain. Austenite unit triangle shown in the right upper corner. Tensile tests were carried out in the direction perpendicular to the growth direction

Figure 11 shows IPF maps from the as-deposited sample (the same area as marked in Figure 10) after 5.6% of in-situ tensile strain (1) and after in-situ 8 % tensile strain (2). The central austenite grain is marked in green color in pictures 1 and 2, while the martensitic needles are marked in grey and blue. The average thickness of plates based on more than 100 measured plates was estimated as 0.9  $\mu\text{m}$ . The average orientation was calculated for each grain group and the misorientation between two average orientations was determined. The misorientation is presented in the axis angle notation, which indicates the smallest angle of rotation around a crystallographic direction to transform the reference frame of the first grain to the reference frame of the second grain. The misorientation relationship was then used to plot specified plane poles as oriented in the second grain in the reference frame of the first grain (coloured markers on the plot). Then, planes in the first grain closest to planes from the second grain were determined and presented with black markers.



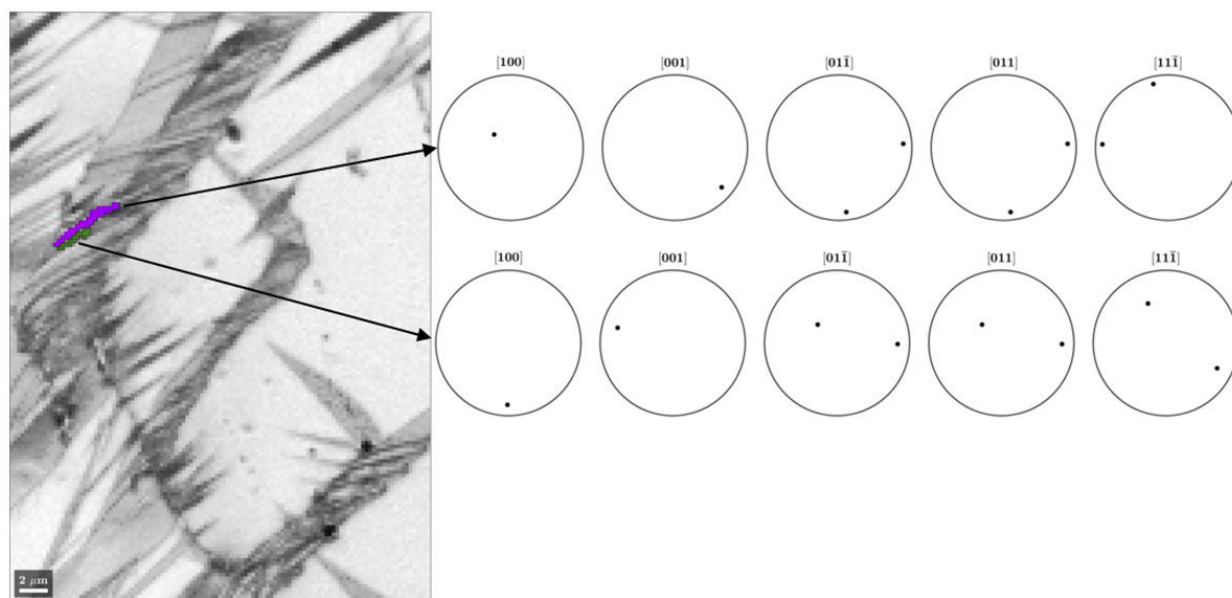
Misorientation angle between closest planes:

$(0\bar{1}1)$ NiTi cubic  $(001)$ NiTi monoclinic  
misorientation angle:  $1.12^\circ$

$(100)$ NiTi cubic  $(100)$ NiTi monoclinic  
misorientation angle:  $2-5^\circ$

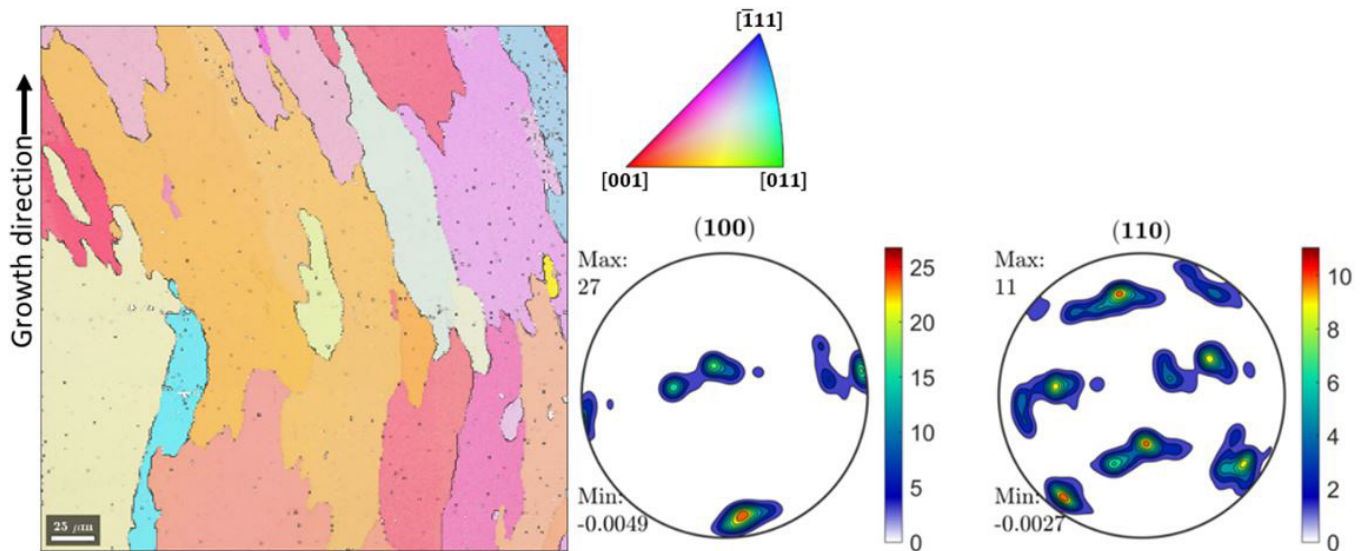
**Figure 11:** IPF maps from the as deposited sample (the same area as marked in Figure 10) after 5,6% of in-situ tensile strain (1) and after in-situ 8 % tensile strain (2). On the right side corresponding pole figures take from the marked needle and nearby austenite in (1) and (2). Below, the stereographic 001 projection of B19' martensite with marked coloured pole positions of austenite

The corresponding pole figures (PF) from the marked area after 5.6% and 8% of strain indicate that the crystallographic planes  $(0\bar{1}1)$  of B2 austenite are parallel to  $(001)$  B19' martensite and the misorientation angle is 1.12 degree as results from the overlapping of corresponding peaks in the pole figures  $001$  B19' and  $110$  B2. Similarly, peaks overlapping can be seen at  $(100)$  PFs of martensite and austenite showing crystallographic relationship as reported earlier  $[100]_{B19'} \parallel [100]_{B2}$  in [26,33] and the misorientation being between 2-5 degrees. Both martensite variants propagate close to  $45^\circ$  to the tensile axis as also observed in earlier in-situ studies [26] due to Schmid factor values, as both martensite plates are close to the  $\{110\}$  planes traces. This effect is particularly well seen in in-situ deformed samples while recording the local temperature increase during deformation [27]. In the micrographs in Figure 11 one can also see that grain boundaries act as barriers for the growth of martensitic needles however they can act also as nucleation sites due to induced stresses, however most often at other orientation corresponding to that of the next grain. It can be better seen at the same area with the strain value increased up to 8% shown in Figure 12, where at higher stress higher density of martensitic needles can be observed. One can see nucleation of several small needles at the grain boundary. In addition within broader needles parallel small plates can be distinguished, being most probably martensite twins as reported earlier [27-31]. The orientations of two of them marked in violet and green colors were analyzed in view of mutual orientation dependence and corresponding pole figures are shown on the right side marked with arrows. One can see from  $(011)$  pole figures that both needles have a common  $(11\bar{1})$  plane what suggests the presence of a type I twin boundary as observed earlier for B19' martensite in NiTi alloys [27-31]. Microstructures reported in TEM studies of  $\{1\bar{1}1\}$  twin boundaries in 3D manufactured NiTi alloys have a similar character, however a compound  $\{100\}$  twins were also observed. Possible type I twins are related to mirror symmetry between the twin and parent grain where the mirror plane can be the one of the following planes:  $(11\bar{1})$ ,  $(001)$ ,  $(100)$  and  $(011)$ ,  $(311, 201)$  [26,32]. Type II twins are connected to rotation symmetry with the  $180^\circ$  rotation around the  $\langle 011 \rangle$  axis [27-29]. At higher deformation as shown in Fig.12 a few needles grow under the angle of  $90^\circ$  (marked by arrows) indicating nucleation of a new variant of martensite occurring at higher stresses. Analysing corresponding pole figures of these plates, compound twins were also observed, where twin exhibits the mirror symmetry with respect to the  $(001)$  plane and  $180^\circ$  rotation symmetry around the  $[100]$  direction [27, 28]. However one cannot exclude that these two orientations formed as a result of the austenite/martensite relationship  $(001)_{B19'} \parallel (01\bar{1})_{B2}$  and  $[100]_m \parallel [100]_a$  coexisting with orientation variant  $(001)_{B19'} \parallel (0-11)_{B2}$  and  $[100]_{B19'} \parallel [00-1]_{B2}$  [3]. The microstructure itself suggest rather the second possibility, since no clear twin boundaries were observed in the microstructure. At the strain of 5.5 % nucleation of martensite plates was observed preferentially at the grain boundaries as also observed earlier during in situ local strain distribution pattern observation using *Confocal Scanning Laser Microscopy* and EBSD techniques [26,32].



**Figure 12:** Magnified micrograph from the area (2) marked in Figure 11 after in-situ strain increase up to 8 %. On the right side pole figures from two (in violet and green colors) martensitic needles most probably in twin orientation

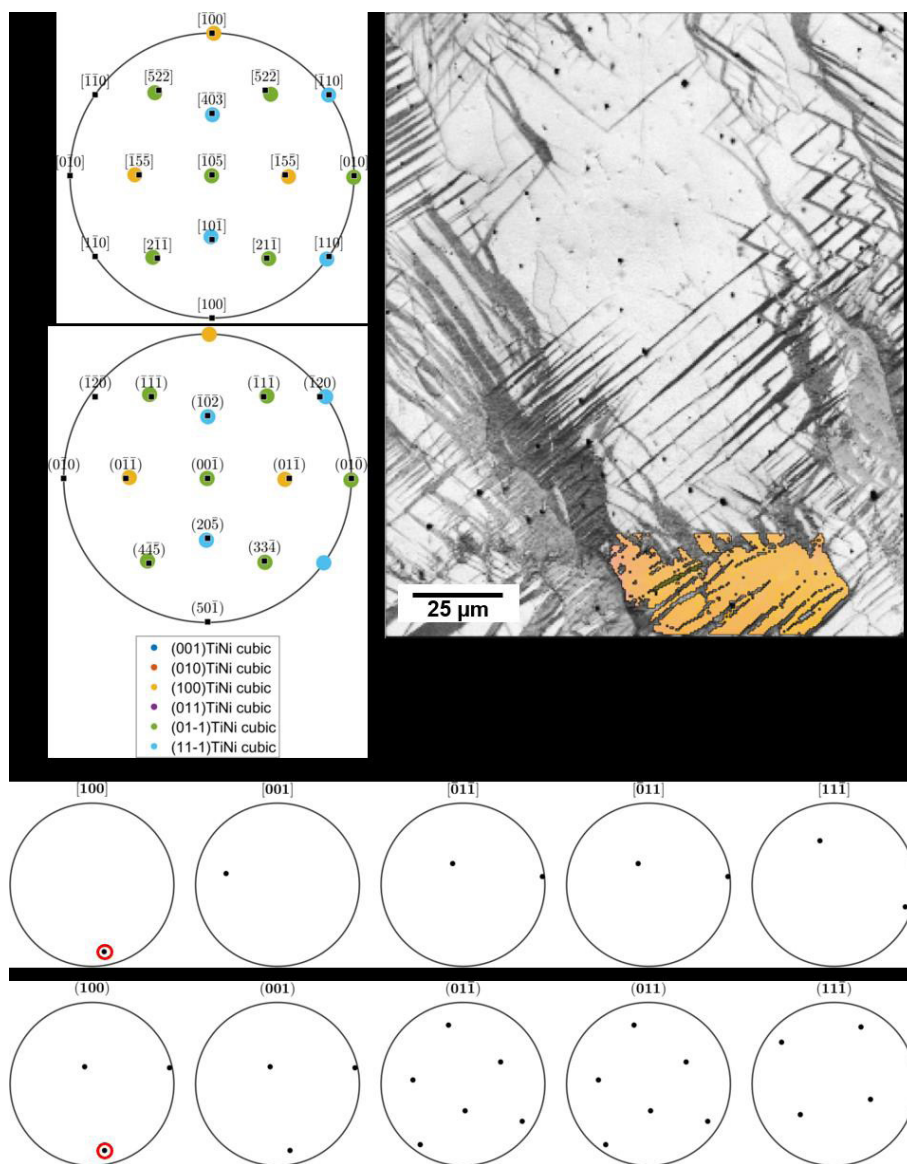
The microstructure of the aged sample deformed in-situ to the same degree of strain was also investigated. Figure 13 shows the initial microstructure and the corresponding (100) (110) pole figures. It shows a similar character to the as-manufactured sample, as the annealing did not change the microstructure and the texture close to [001].



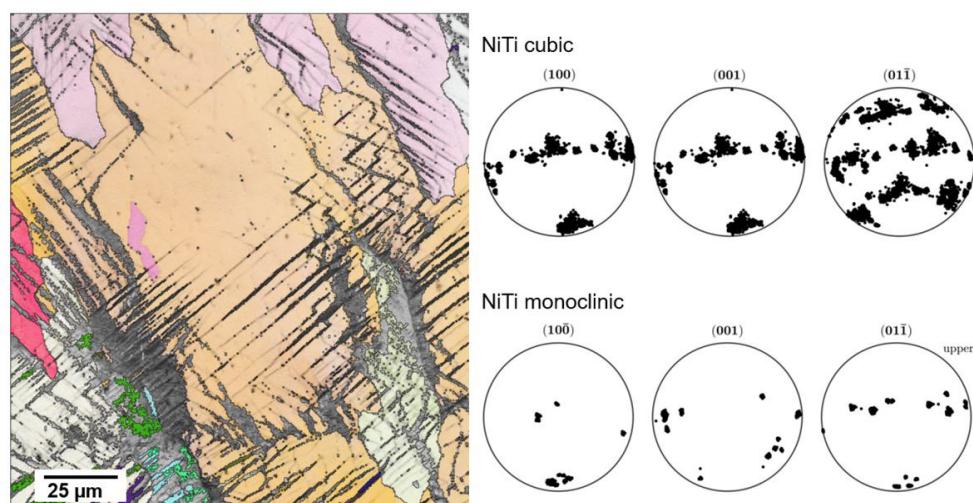
**Figure 13:** IPF map and (100) and (110) pole figures of as manufactured and aged 2h/500°C NiTi sample, measured perpendicularly to the growth direction marked by an arrow. Tensile tests were carried out in the direction perpendicular to the growth direction

Figure 14 shows SEM microstructure of the sample aged 2h/500°C tensile strained 5.6%. It shows rather narrow needles (of the average thickness of 1.15 $\mu$ m) formed preferentially under angles near 45°. Some of them show a zig-zag character as also observed during in-situ observation in [26]. At the bottom of the micrograph a coloured fragment can be seen where individual orientations of martensite plates and austenite grain were measured. There are shown two examples of stereographic projections of martensite with the observed orientation relationships between cubic austenite and monoclinic phase like  $[010]_{B2} \parallel [100]_{B19'}$  (angle: 0.70);  $[001]_{TiNi_{B2}} \parallel [1\bar{3}3]_{NiTi_{B19'}}$  (angle: 4.28);  $[001]_{TiNi_{B2}} \parallel [011]_{B19'}$  (angle: 6.03),  $[100]_{B2} \parallel [011]_{B19'}$  (angle: 5.38),  $[11-1]_{B2} \parallel [-110]_{B19'}$  (angle: 1.61) and  $[011]_{B2} \parallel [2\bar{1}1]_{B19'}$  (angle: 1.66). Most of them were reported to exist between these phases except higher order reflections like [133], [445] monoclinic, which may result from the planes rotation due to plastic deformation (causing manifested differences of a few degrees marked in crystallographic relationships) resulting from stress localization as observed in in-situ studies [26,32]. At the bottom of Fig.14 are shown pole figures PF from austenite and B19' martensite, where one of the orientation relationship  $[010]_{B2} \parallel [100]_{B19'}$  is presented.

Figure 15 shows an IPF map and (100), (001) and (01 $\bar{1}$ ) PFs (with marked individual orientations due to a small number of crystals) from the sample aged 2h/500°C strained to 5.6%. It shows a similar character of nucleated needles with martensitic formed first at an angle close to 45° due to Schmid factor values, similarly to that in the as-deposited sample. Some areas, particularly near grain boundaries and martensitic needles, are in grey color and they represent areas of unsolved orientations. Their relatively large number in comparison to the as-prepared sample is most probably due to the presence of fine precipitates causing additional strain field and weak diffraction lines. Pole figures from the cubic phase are similar to those in the initial sample in Figure 13, however a new orientation appears in the initial PF as compared to the case of as-deposited samples due to the formation of new orientations. Nevertheless it was possible to measure single orientations of cubic/monoclinic relationship in some places (particularly at the bottom of the micrograph) as presented in Figure 14. Comparison of peak positions indicates the possibility of a large number of orientation relationships similarly



**Figure 14:** SEM micrograph and at the bottom IPF map from the deposited and aged 2h/500°C sample after 5.6% of in-situ tensile strain. On the left side corresponding stereographic projections of measured B2/B19' orientation relationships and below 100, 001, 01-1, 011, 11-1 PF from cubic (upper) and monoclinic phase (below)



**Figure 15:** (a) IPF map and corresponding (100) and (100) and (011) pole figures of cubic austenite and B19' martensitic phase in LENS manufactured and aged 2h/500°C NiTi sample deformed in-situ 5.6%. PF correspond to the austenitic phase marked red, rose and grey and martensite in blue and green colours

Figure 16 shows an IPF map and (100), (001) and (011) PF from the sample aged 2h/500°C strained 8 % of in-situ tensile strain. One can see that the unsolved areas (marked in grey) are much larger than that after 5.6% of strain, most probably due to much larger inhomogeneity of strain agglomeration resulting in a poor diffraction line quality. However, the orientations were measured from a small area, and formation of new orientation peaks of austenitic and martensitic phases most probably are the result of larger plastic deformation. Comparison of individual orientations of the parent and martensitic phases shows the presence of the earlier observed relationship  $(001)_{B19'} \parallel (01-1)_{B2}$  and  $[100]_{B19'} \parallel [100]_{B2}$ .

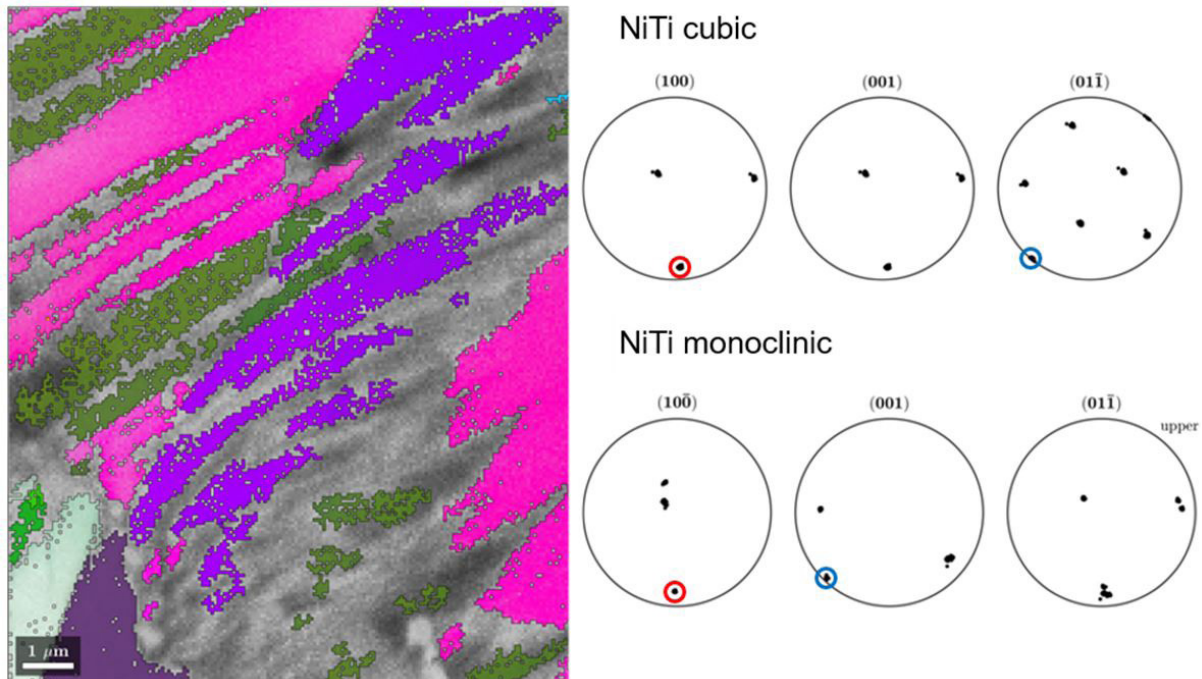


**Figure 16:** IPF map and corresponding 100, 001 and  $01\bar{1}$  pole figures of cubic austenite and B19' martensitic phase in LENS manufactured sample aged 2h/500°C and deformed in-situ 8%. In the IPF map austenitic and martensitic phases are marked by purple, violet and green colours respectively, while grey indicate unsolved areas

## Conclusions

1. Samples for in-situ tensile experiment prepared using the LENS method showed strong texture near  $\langle 001 \rangle$  parallel to the build direction. At grain boundaries they contained intermetallic particles of size 0.5-2  $\mu\text{m}$  identified as  $\text{Ti}_2\text{Ni}$  and  $\text{Ti}_2\text{Ni}_3$  identified using EDS analysis and TEM diffraction. The simultaneous formation of Ti rich and Ni rich precipitates may be caused by a local oxidation of titanium. The as deposited sample showed diffused DSC peaks corresponding to martensitic transformation with  $M_s = 4^\circ\text{C}$  and  $A_f = 32^\circ\text{C}$ . It has shown a good superelastic properties at RT, however after 4% strain a residual strain of 0.7% was observed. The residual strain decreased when the deformation temperature was lifted up to 43°C i.e. above  $A_f$ .
2. The alloy aged at 500 °C, even after short time of annealing, shows an additional peak corresponding to  $R \rightarrow B19'$  phase transformation, during cooling and reverse transformation  $B19' \rightarrow R$  on heating. The martensitic transformation temperatures and the reverse transformation both increase with the ageing time and after 2 hours of ageing at 500 °C reach values of  $M_s = 5^\circ\text{C}$  and  $A_f = 43.5^\circ\text{C}$ . Straining at RT caused reorientation and deformation of martensite and possible shape recovery above  $A_s$ , and at 53 °C superelastic properties were observed.  $\text{Ni}_4\text{Ti}_3$  precipitates were identified after 2 hours of ageing.
3. In-situ tensile deformation of LENS deposited sample causes nucleation of martensitic plates first at the surface of samples; then plates nucleate preferentially at grain boundaries and propagate across grains. From the PFs measurements the following crystallographic relationships were most frequently observed:  $(001)_{B19'} \parallel (01-1)_{B2}$  and  $[100]_{B19'} \parallel [100]_{B2}$ , however other variants were also present. From the microstructures and distribution of peaks in PFs the existence of martensite twins on (110) and  $(10\bar{2})$  planes was observed. No twins in austenite were found in the microstructures.

4. In-situ tensile deformation of LENS deposited samples aged 2h/500°C causes a decrease of plate thickness from 1.15  $\mu\text{m}$  to 0.9  $\mu\text{m}$ , what suggests the participation of strain field near  $\text{Ni}_4\text{Ti}_3$  precipitates in more frequent nucleation of martensitic plates. Furthermore, a large variety of crystallographic orientation relationships between cubic austenite phases like  $[010]_{\text{B}_2} \parallel [100]_{\text{B}_{19}'}$  (angle: 0.70);  $[001]_{\text{B}_2} \parallel [1\bar{3}3]_{\text{B}_{19}'}$  (angle: 4.28);  $[001]_{\text{B}_2} \parallel [011]_{\text{B}_{19}'}$  (angle: 6.03),  $[100]_{\text{B}_2} \parallel [011]_{\text{B}_{19}'}$  (angle: 5.38),  $[11\bar{1}]_{\text{B}_2} \parallel [\bar{1}10]_{\text{B}_{19}'}$  (angle: 1.61);  $[011]_{\text{B}_2} \parallel [\bar{2}\bar{1}1]_{\text{B}_{19}'}$  (angle: 1.66) were observed. Based on SEM observation and PF analysis some twin orientations were identified in martensite particularly at higher deformation of 8%.

## Acknowledgments

The presented research results are the effect of the project no. UMO-2016/23/B/ST8/00754 financed by the National Science Center, Poland and the additive manufacturing process was funded by the statutory sources of the Department of Material Technologies, Military University of Technology. The authors are grateful to dr M. Chandrasekaran from SMATEC Company, Belgium for valuable discussions and supplying the NiTi wire and support sheets.

Partial financial support from the Spanish AEI and EU-FEDER, research project RTI2018-094683-B-C51, is acknowledged.

## Reference

1. JV Humbeeck, Y Liu (2000) Shape memory alloys as damping materials, *Materials science forum* 327-328, 331-338.
2. T Yoneyama, S Miyazaki (2010) Shape memory alloys for biomedical applications, Woodhead Publishing Ltd, Cambridge.
3. IV Shishkovsky, IA Yadroitsev, IY Smurov (2013) Manufacturing three-dimensional nickel titanium articles using layer-by-layer laser-melting technology, *Technical Physics Letters* 39: 1081-4.
4. RF Hamilton, BA Bimber, TA Palmer (2018) Correlating microstructure and superelasticity of directed energy deposition additive manufactured Ni-rich NiTi alloys, *Journal of Alloys and Compounds*. 739: 712-722.
5. I Gibson, D Rosen, B Stucker (2015) Additive Manufacturing Technologies: 3D Printing, Rapid Prototyping, and Direct Digital Manufacturing, Springer, New York.
6. JP Oliveira, AJ Cavaleiro, N Schell, A Stark, ARM Miranda (2018) Effects of laser processing on the transformation characteristics of NiTi: A contribute to additive manufacturing, *Scripta materialia* 152: 122-6.
7. T Bormann, R Schumacher, B Müller, N Mertmann, M de Wild (2012) Tailoring selective laser melting process parameters for NiTi implants, *Journal of Materials Engineering and Performance*. 21: 2519-24.
8. S Saedi, AS Turabi, MT Andani, C Haberland, H Karaca, et al. (2016) The influence of heat treatment on the thermomechanical response of Ni-rich NiTi alloys manufactured by selective laser melting. *J Alloys and Compounds*. 677: 204-10.
9. C Ma, D Gu, D Dai, M Xia, H Chen (2018) Selective growth of  $\text{Ni}_4\text{Ti}_3$  precipitate variants induced by complicated cyclic stress during laser additive manufacturing of NiTi-based composites, *Materials Characterization*. 143: 191-6.
10. JJ Marattukalam, VK Balla, M Das, S Bontha, SK Kalpathy (2018) Effect of heat treatment on microstructure, corrosion, and shape memory characteristics of laser deposited NiTi alloy, *Journal of Alloys and Compounds*. 744: 337-46.
11. S Kumar, L Marandi, VK Balla, S Bysakh, D Piorunek, et al. (2019) Microstructure-property correlations for additively manufactured NiTi based shape memory alloys. *Material* 8: 100456.

12. Z Zeng, JP Oliveira, S Ao, W Zhang, J Cui, et al. (2020) Fabrication and characterization of a novel bionic manipulator using a laser processed NiTi shape memory alloy. *Optics & Laser Technology*, 2020, 122, 105876.
13. J Wang, Z Pan, Y Wang, L Wang, S Su, et al. (2020) Evolution of crystallographic orientation, precipitation, phase transformation and mechanical properties realized by enhancing deposition current for dual-wire arc additive manufactured Ni-rich NiTi alloy, *Additive Manufacturing*. 34: 101240.
14. J Dutkiewicz, L Rogal, D Kalita, M Węglowski, S Błacha, et al. (2020) Superelastic effect in NiTi alloys manufactured using electron beam and focused laser rapid methods, *Journal of Materials Engineering and Performance*. 29: 4463-73.
15. M Elahinia, NS Moghaddam, MT Andani, A Amerinatanzi, BA Bimber, et al. (2016) Fabrication of NiTi through additive manufacturing: A review. *Progress in Materials Sci* 83: 630-63.
16. S Saedi, AS Turabi, MT Andani, NS Moghaddam, M Elahinia, et al. (2017) Texture, aging, and superelasticity of selective laser melting fabricated Ni-rich NiTi alloys, *Materials Science and Engineering: A*, 2017, 686, 1-10.
17. C Elibol, MFX Wagner (2015) Investigation of the stress-induced martensitic transformation in pseudoelastic NiTi under uniaxial tension, compression and compression–shear, *Materials Science and Engineering: A* 621: 76-81.
18. SC Mao, JF Luo, Z Zhang, MH Wu, Y Liu, et al. (2010) EBSD studies of the stress-induced B2–B19' martensitic transformation in NiTi tubes under uniaxial tension and compression, *Acta Materials* 58: 3357-66.
19. G Laplanche, T Birk, S Schneider, J Frenzel, G Eggeler (2017) Effect of temperature and texture on the reorientation of martensite variants in NiTi shape memory alloys. *Acta Materials* 127: 143-52.
20. A Kröger, R Wernhardt, C Somsen, G Eggeler, A Wieck (2006) In situ transmission electron microscopy-investigations on the strain-induced B19'-phase in NiTi shape memory alloys structured by focused ion beam. *Materials Science and Engineering: A* 438-440, 513-516.
21. S Manchuraju, A Kroegeer, C Somsen, A Dlouhy, G Eggeler, et al. (2012) Pseudoelastic deformation and size effects during in situ transmission electron microscopy tensile testing of NiTi. *Acta materials* 60: 2770-7.
22. H Morawiec (2014) *Shape memory metals and their application* (in Polish), Publishing House of the University of Silesia, Katowice.
23. I Kaya, HE Karaca, M Nagasako, R Kainuma (2020) Effects of aging temperature and aging time on the mechanism of martensitic transformation in nickel-rich NiTi shape memory alloys, *Materials Characterization* 159: 110034.
24. J Khalil Allafi, G Eggeler, WW Schmahl, D Sheptyakov (2006) Quantitative phase analysis in microstructures which display multiple step martensitic transformation in Ni-rich NiTi shape memory alloys. *Mater Sci Eng A* 438-40, 593-6.
25. Y Xiao, P Zeng, L Lei, Y Zhang (2017) In situ observation on temperature dependence of martensitic transformation and plastic deformation in superelastic NiTi shape memory alloy, *Materials & Design* 134: 111-20.
26. E Polatidis, M Smíd, I Kubena, WN Hsu, G Laplanche, et al. (2020) Deformation mechanisms in a superelastic NiTi alloy: An in-situ high resolution digital image correlation study. *Materials & Design* 191: 108622.
27. C. Cayron (2020) What EBSD and TKD Tell Us about the Crystallography of the Martensitic B2-B19' Transformation in NiTi Shape Memory Alloys, *Crystals* 10: 562.

- 
28. S Pfeiffer, MFX Wagner (2017) Elastic deformation of twinned microstructures, *Proceedings of the Royal Society A: Mathematical, Physical and Eng Sci* 473: 20170330.
29. Q Zhang, S Hao, Y Liu, Z Xiong, W Guo, et al. (2020) The microstructure of a selective laser melting (SLM)-fabricated NiTi shape memory alloy with superior tensile property and shape memory recoverability, *Applied Materials Today* 19: 100547.
30. P Sittner, L Heller, J Pilch, C Curfs, T Alonso, et al. (2014) Young's modulus of austenite and martensite phases in superelastic NiTi wires, *Journal of materials engineering and performance* 23: 2303-14.
31. A Radi, J Khalil-Allafi, MR Etmianfar, S Pourbabak, D Schryvers, et al. (2018) Influence of stress aging process on variants of nano-Ni<sub>4</sub>Ti<sub>3</sub> precipitates and martensitic transformation temperatures in NiTi shape memory alloy, *Materials and Design* 142: 93–100.
32. J Lackmann, T Niendorf, M Maxisch, G Grundmeier, HJ Maier (2011) High-resolution in-situ characterization of the surface evolution of a polycrystalline NiTi SMA-alloy under pseudoelastic deformation, *Materials Characterization* 62: 298-303.
33. VV Martynov (1995) X-ray diffraction study of thermally and stress-induced phase transformations in single crystalline Ni-Mn-Ga alloys, *Le J de Physique IV* 5: C8, C8-91 – C8-99.
34. Y Chen, O Molnarova, O Tyc, L Kaderavek, L Heller, (2019) Recoverability of large strains and deformation twinning in martensite during tensile deformation of NiTi shape memory alloy polycrystals, *Acta Materialia* 180: 243–59.